Journal of Drug Delivery Science and Technology 114 (2025) 107558

Contents lists available at ScienceDirect

Journal of Drug Delivery Science and Technology

journal homepage: www.elsevier.com/locate/jddst

3D-printed biopolymer matrices for the vehiculization and controlled release of octenidine in wound antibiotic therapy

Ignacio Rivero Berti [a,b], Manuel Horue [a], Tugce Boztepe [a], Marcelo Calderón [c,d], Luciano Mengatto [e], Stephan Gehring [b], Sergio Katz [a], Germán Islan [a,b,*], Federico Karp [a,**]

[a] Centro de Investigación y Desarrollo en Fermentaciones Industriales (CINDEFI), Laboratorio de Nanobiomateriales, Departamento de Química, Facultad de Ciencias Exactas, Universidad Nacional de La Plata (UNLP) -CONICET (CCT La Plata), Calle 47 y 115, (B1900AJI), La Plata, Buenos Aires, Argentina
[b] Children's Hospital, University Medical Center of the Johannes-Gutenberg University, Langenbeckstr. 1, 55131 Mainz, Germany
[c] 55131 POLYMAT, Applied Chemistry Department, Faculty of Chemistry, University of the Basque Country UPV/EHU, Paseo Manuel de Lardizabal 3, 20018, Donostia-San Sebastián, Spain
[d] IKERBASQUE, Basque Foundation for Science, Plaza Euskadi 5, 48009, Bilbao, Spain
[e] Instituto de Desarrollo Tecnológico para La Industria Química, INTEC (Universidad Nacional Del Litoral and CONICET), Güemes 3450, Santa Fe, 3000, Argentina

ARTICLE INFO

Keywords:
3D-printing
Alginate
Carboxymethyl chitosan
Octenidine
pH-sensitive
Antimicrobial

ABSTRACT

Chronic and acute wounds are important health system problems due to re-hospitalization rates and treatment engagement. Antibiotic-controlled release systems can be a relevant solution for generating long-term therapies without patient intervention. The present work investigated pH-sensitive biopolymeric systems obtained by extrusion-based 3D printing. Alginate and carboxymethyl chitosan were used as matrix polymers for ink production, while octenidine was the vehiculized antibiotic. Different polymer proportions were explored to evaluate the release mechanism in response to different pH environments. Physicochemical characterization was performed using infrared spectrometry (FTIR) and thermogravimetric analysis (TGA). Detailed photography was used to determine 3D-printing fidelity. SEM images were used for the morphological characterization. Swelling and octenidine release profiles were evaluated in different non-chelating buffers. After the print's crosslinking bath, the obtained encapsulation efficiency was 100 %. The printing fidelity was in the order of 0.9–1.8. Swelling studies showed that some formulations lost weight, whereas others increased by 400 %. After 7 days, the drug released was 20–85 %, depending on the polymer composition and buffer/pH environment. All the prints presented antimicrobial capacity against *Staphylococcus aureus*. The present work demonstrates the potential of biopolymeric 3D-printed systems as advanced wound dressings, combining pH-responsive antibiotic release and antimicrobial activity with the adaptive design capabilities of 3D printing, offering a versatile platform for personalized wound-healing therapies.

1. Introduction

Wounds are disruptions of epithelial tissue that alter its normal structure and function. Specifically, in cutaneous wounds, skin disruption occurs as a consequence of physicochemical and/or biological damage or pathophysiological disorders [1,2]. Wounds can be classified as acute or chronic depending on healing time. Acute wounds (AW), caused by mechanical, electrical, heat, radiation, or chemical sources, typically heal within a reasonable timeframe, normally less than 12 weeks and usually require a simple treatment [2,3]. In contrast, chronic wounds (CW) fail to heal in the expected timeframe, representing a significant burden on patients and health systems [4]. Moreover, it is estimated that between 1 % and 2 % of the population in developed countries will experience CW during their lifetime, particularly due to aging, diabetes, and obesity, the main key risk factors for impaired healing [5]. This burden is reflected in the wound care market, where the global chronic wound care segment is projected to grow faster than the acute wound market, reaching USD 25.22 billion by 2032,

* Corresponding author. Children's Hospital, University Medical Center of the Johannes-Gutenberg University, Langenbeckstr. 1, 55131 Mainz, Germany.
** Corresponding author. Centro de Investigación y Desarrollo en Fermentaciones Industriales (CINDEFI), Laboratorio de Nanobiomateriales, Departamento de Química, Facultad de Ciencias Exactas, Universidad Nacional de La Plata (UNLP) -CONICET (CCT La Plata), Calle 47 y 115, (B1900AJI), La Plata, Buenos Aires, Argentina.
E-mail addresses: germanis@uni-mainz.de (G. Islan), federicokarp@gmail.com (F. Karp).

https://doi.org/10.1016/j.jddst.2025.107558
Received 23 June 2025; Received in revised form 14 September 2025; Accepted 20 September 2025
Available online 23 September 2025

presenting a CAGR of 7.4 % between 2025 and 2032 [6–8].

Traditional wound dressings such as gauze, mainly act as passive physical barriers between the injured site and the environment and are insufficient for complex wounds, particularly CW. Advanced systems or active wound dressings aim to provide a favorable healing environment by controlling the progression of infection, maintain hydration while absorbing exudate, and be highly biocompatible [9]. The addition of antimicrobial or bioactive agents is often required, and controlled drug delivery systems can improve both treatment effectiveness and compliance by providing sustained release over time [10]. Importantly, the pH plays a regulatory role in healing: healthy skin is acidic (pH 4.5–5.3), but wounds shift towards values closer to the physiological pH of the *milieu intérieur* (7.4). As the wound heals, it gradually acidifies to a normal pH while CW often remain alkaline, preventing proper wound healing [11].

Hydrogels are promising materials for smart pH-responsive wound dressings, not only due to their pH responsiveness but also due to their high water retention capacity, mechanical properties, and biocompatibility [9,12]. Recent advances in 3D printing technologies further expand their potential. Different materials, biopolymers, or combinations of these to formulate the ink can be used to mimic the natural wound microenvironment and provide tailored support for tissue regeneration and repair. [13]. In addition, this technology can produce customized wound dressings in terms of porosity, hydration rate and geometry to match tissue defects, enabling personalized treatment and better integration with the wound site. Loading of antimicrobial or bioactive agents becomes a necessity, and 3D printing can be used to address this issue [14]. 3D printing based on additive manufacturing by extrusion enables fabrication of hydrogel drug delivery systems at mild conditions and room temperature and without radiation, avoiding the degradation of thermosensitive drugs or biopolymers. Other methods of 3D-printing such as fused deposition modeling (FDM) and stereolithography (SLA) are widely used for thermoplastic and photopolymer processing, respectively, but they require conditions (high temperature or UV curing) that can degrade sensitive biomolecules [15,16]. In 2015, the first 3D printing-based drug, Spritam®, was approved by the FDA, and since then, the number of new products only increased, with fast-track approvals for new drug formulations already on the market demonstrating the translational potential of 3D printing in drug delivery [17–19].

Common materials employed in 3D printing include hydrogels, biopolymers, synthetic polymers, and natural biomaterials such as decellularized extracellular matrix (dECM) [20]. Calcium alginate (ALG) has been widely used in hydrogel patches, due to its biocompatibility, biodegradability, non-immunogenicity, and high aqueous absorption capacity, along with a well-described pH-dependent swelling behavior [21]. Fayyazbakhsh et al. developed a printed hybrid hydrogel with a ratio of 75 % gelatin and 25 % alginate that offers an optimal balance between mechanical properties, hydration and biocompatibility, promoting faster and more effective healing compared to non-printed hydrogels and standard dressings [22]. Cleetus et al., fabricated alginate hydrogels impregnated with zinc oxide nanoparticles by 3D printing, with higher structural stability, homogeneous porosity, and moisture retention capacity compared to manually molded hydrogels, in combination with antimicrobial properties [23]. Huang et al. developed 3D-printed smart alginate dressings incorporating calcium phosphate nanoparticles to enable pH-dependent, controlled release of antimicrobials and nanoparticles [24]. The dressings were designed to respond to elevated pH levels in infected wounds, releasing therapeutic agents more rapidly in alkaline conditions while reducing release in healthy tissues.

Carboxymethyl chitosan (CMCh) has also many attractive properties for the formation of dressings, such as its hemostatic properties and high biocompatibility. However, unlike chitosan, it has the additional advantage of being water-soluble [25]. A few works on 3D-printed CMCh-based systems for wound treatment can be found in the bibliography. Naseri et al. produced hybrid biomaterial inks based on starch and N,O-CMCh for 3D printing of biodegradable wound dressings for the release of mupirocin, a topical anti-infective drug. The results showed that N,O-CMCh/starch ratio affects drug release, flexibility of the films and antibacterial efficacy [26]. García et al. developed an innovative protocol for the fabrication of 3D CMCh scaffolds by additive manufacturing crosslinked by Zn2+, intended for applications as antimicrobial dressings for skin regeneration [27]. In a second step, the scaffolds were functionalized with collagen to increase the ability of support fibroblast viability *in vitro* and accelerate the wound healing process.

Recent studies also have explored 3D-printed hydrogel dressings for wound healing. Kim et al. demonstrated that DNA-induced biomineralization in a 3D-printed hydrogel accelerated diabetic wound healing by enhancing tissue regeneration [28]. Tsegay et al. developed a 3D-printed auxetic hydrogel incorporating a pH indicator, enabling visual monitoring of wound environment changes [29]. Bergonzi et al. fabricated chitosan/alginate hydrogels for controlled release of silver sulfadiazine, achieving effective antimicrobial activity while supporting wound healing [30]. Huang et al. produced smart 3D-printed alginate dressings with pH-responsive release of drugs and nanoparticles according to different wound conditions [31].

While all those studies highlighted promises advances in 3D-printed hydrogels for wound care, few systems integrate fully biopolymeric matrices with pH-responsive and sustained release of clinically relevant antiseptics.

Octenidine (OCT) is an antiseptic and cationic surfactant bispyridine and one of the main active components widely used in CW management. It is stable and active over a wide pH range, shows a broad antibacterial spectrum, is less cytotoxic than silver-based alternatives and exhibits no toxic effects on human epithelial cells at the active concentrations [32–34]. OCT has demonstrated clinical superiority in terms of wound size reduction, cytokine profile, granulation, and re-epithelialization [34–37]. Nevertheless, direct application of OCT may induce local adverse effects, including burning sensations, erythema, pruritus, and dryness, motivating its encapsulation within a patch-based delivery system.

Attempts to create a biocompatible dressing, including OCT as an active component, are numerous, involving both organic and inorganic materials [38–40]. However, to the best of our knowledge, only one published study has investigated a system based on 3D printing and mainly focused on the thermoresponsive properties of the prints for the release of Octisept®, a mixture containing OCT and phenoxyethanol [41].

Based on this context, we developed alginate/CMCh-based 3D-printed drug delivery systems for the pH-dependent OCT delivery, based on the individual ionic equilibrium of the components (Fig. 1). Our study evaluates physicochemical properties, swelling behavior, drug release kinetics, and antimicrobial performance, highlighting the potential of extrusion-based 3D printing as a platform for personalized, infection-responsive, fully biopolymeric wound dressings.

2. Materials and methods

2.1. Materials

O-Carboxymethyl-chitosan (CMCh) with a deacetylation degree of 90 % was purchased from Santa Cruz Biotechnology (TX, USA). Sodium alginate (ALG) ($\overline{M}_W = 120$ kDa) was provided by Monsanto (MO, USA). Octenidine dihydrochloride (OCT) was obtained from Glentam (Corsham, UK). All other reagents were of analytical grade and obtained from available commercial sources. Ultrapure water was obtained from a DirectQ-3 water purification system (Merck Millipore, MA, USA). Mueller-Hinton Agar medium was purchased from Britania Laboratories (CABA, Argentina).

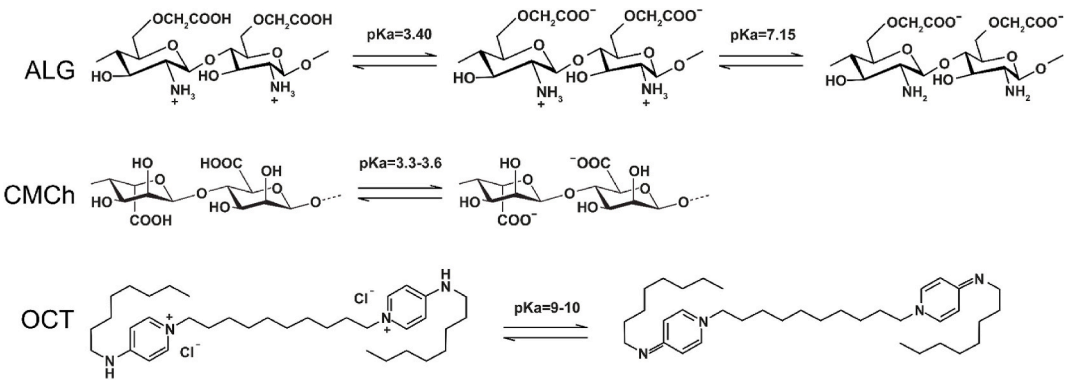

Fig. 1. Ionic equilibria of the substances used in this work.

2.2. Biopolymer-ink preparation

To prepare the inks, weighted amounts of CMCh, ALG, and ultrapure water were mixed to obtain a 9 % (w/w) biopolymer concentration. The proportions of ALG-CMCh were 100-0, 75–25, 50-50, 25–75, and 0–100, and named 100_{ALG}-0_{CMCh}, 75_{ALG}-25_{CMCh}, 50_{ALG}-50_{CMCh}, 100_{ALG}-0_{CMCh}. The inks were then homogenized in a DISPERMAT® LC-EX (VMA-GETZMANN, Germany) at 500–8000 rpm using a 50 mm dissolver disk. First, OCT was added to reach a proportion of 0.5 g per 100 g of biopolymer. Subsequently, 800 μL of 0.5 M $CaCl_2$ solution was added dropwise to achieve a printable consistency. All steps were performed using continuous homogenization. The final product was weighed to adjust for water evaporation and stored in a wet-sealed container to prevent moisture loss.

2.3. 3D-structures printing

Biopolymer inks were loaded into 5 mL syringes (Luer-Lock, TERUMO®, Philippines) and centrifuged at 5000 rpm for 5 min in an RC5C Sorvall® centrifuge equipped with an HS-4 rotor to remove air bubbles.

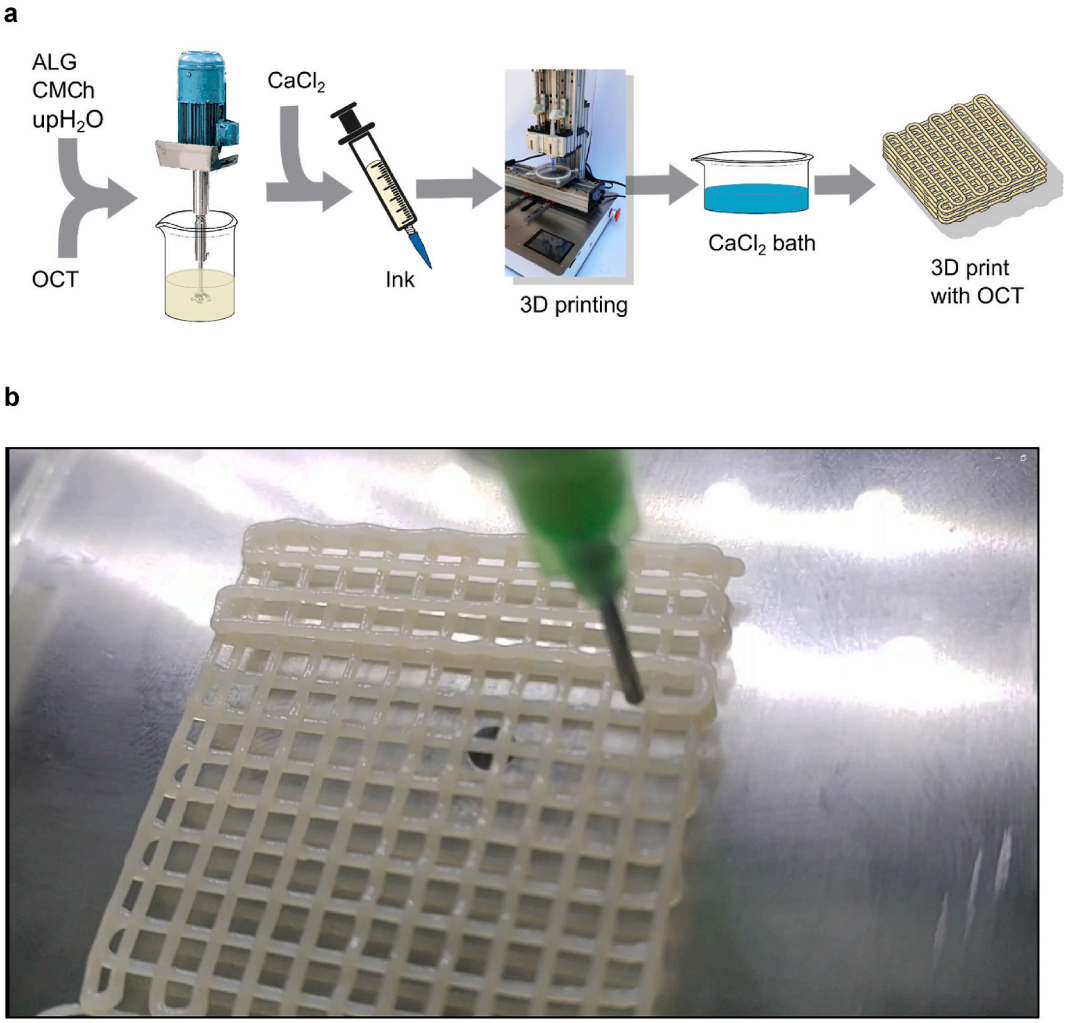

Fig. 2. 3D inks and prints preparation workflow (a) and video of the 3D-printing process (b).

Prints were performed by biopolymer-ink extrusion through a 0.83 mm stainless-steel tip (Nordson EFD, USA) and using a 3D printer designed by the authors [15]. The G-code prints are provided in the supplementary material (Table S1).

Immediately after finishing, the prints were submerged in a 2M $CaCl_2$ solution to complete crosslinking. After 5 min, the prints were washed twice with abundant ultrapure water. Aliquots of the $CaCl_2$ bath and every ultrapure wash were saved to determine the OCT concentration and subsequently calculate the encapsulation efficiency. A schematic and a video of the 3D printing process is shown in Fig. 2.

2.4. Morphological characterization

2.4.1. Photographs and fidelity studies

Images of the 3D prints were captured using a conventional camera (Sony E 16-50 mm f/3.5–5.6 Oss, Sony ILCE-6000, Sony, Japan) with the help of a tripod. Zenithal photos, that is, vertically from top to bottom, were then analyzed using ImageJ® software. The area of the gaps (GapA) delimited by four traces forming squares in the printed meshes (blue squares in Fig. 3) was measured. For each polymer proportion, 35 squares were measured before and after immersion in calcium chloride, resulting in a total of 350 measurements.

2.4.2. Scanning electron microscopy (SEM)

The samples were examined using a Zeiss CrossBeam 350 Scanning Electron Microscope equipped with an Oxford Ultim Max 100 energy-dispersive system. This system allows for elemental chemical analysis via X-ray. The technique, known as Electron Probe Microanalysis (EPMA) using X-rays, can detect only those elements with atomic numbers between 5 (boron) and 98 (californium), inclusive.

Observations and image captures were performed under secondary electron imaging mode at an acceleration voltage of 1 kV, with analyses conducted at 5 kV. In order to estimate surface smoothness from SEM images a grey histogram was created, and a standard deviation from average grey value obtained using ImageJ® software [42]. The spread, or standard deviation of grey values can be correlated with a relative roughness or smoothness of a surface [43].

2.5. Chemical interactions studies

2.5.1. Fourier-transform infrared spectroscopy (FTIR)

Infrared spectra were obtained using a Nicolet 480 FTIR spectrometer (Thermo Fisher Scientific, United States). A MIRacle single reflection attenuated total reflection (ATR) accessory and a diamond prism were used. Each spectrum was measured by recording 64 scans from 4000 to 525 cm^{-1} with a resolution of 4 cm^{-1}. The Advanced ATR Correction feature of EZ Omnic software was used for processing the results and analysis.

2.5.2. Thermogravimetric analysis (TGA)

Thermogravimetric analyses (TGA) were performed using a Q500 TGA instrument (TA Instruments, United States). The measurements were carried out from room temperature to 600 °C. The temperature ramp was set to 10 °C/min. The atmosphere used was N_2 (99.999 % purity, supplied by INDURA) at a flow rate of 100 mL/min. Masses in the range of 4–5 mg were placed in a 100-μL platinum capsule. The temperature of the equipment was calibrated using the Curie temperature of a standard copper sample provided by TA Instruments. Curve analyses were performed using TA Universal V4.5A software.

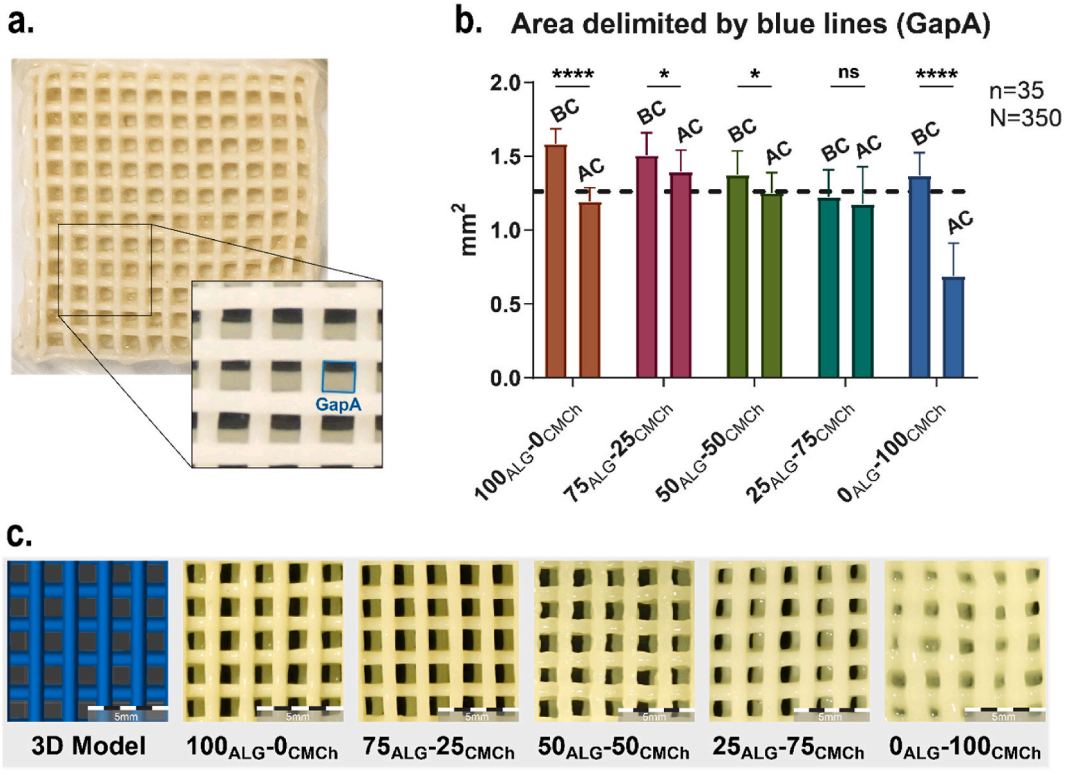

Fig. 3. a. Top view of a complete 3D print. Detail shows area measured as "GapA" **b.** Area delimited by four strokes of the 3D printer (blue square in 3**a.**). The dotted line represents the area of the 3D model used to produce the print. Measurements corresponding to the 3D print before the calcium chloride bath are indicated as "BC" and measurements taken afterwards as "AC". Asterisks indicate significance with $p < 0.05$ (*) and $p < 0.0001$ (****). **c.** Details of top-view photographs of 3D prints made with different polymer proportions, as well as the 3D model used to print them. (For interpretation of the references to colour in this figure legend, the reader is referred to the Web version of this article.)

2.6. Swelling studies

Swelling kinetics were studied submerging weighted 3D prints of each composition in 50 ml of three different non-calcium-chelating buffers: pH 5.5 MES [2-(N-morpholino)ethanesulfonic acid] buffer, pH 7.4 TRIS (Tris (hydroxymethyl)aminomethane) buffer, or pH 8.9 glycine buffer at 37 °C. 3D prints were removed at previously defined times, dried 5 s with a paper towel to remove excess buffer and weighted again.

2.7. Drug quantification method and in vitro drug release profiles

OCT quantification was performed by measuring the absorbance in a TECAN Infinite 200 PRO plate reader (Crailsheim, Germany) at λ_{max} = 282 nm. The encapsulation efficiency was determined using an indirect method. The unencapsulated amount of OCT in the $CaCl_2$ baths and wash water were measured and then deducted from the amount of OCT that was initially added.

To evaluate the release kinetics, 3D prints were immersed in 50 mL of fresh pH 5.5 MES buffer, pH 7.4 TRIS buffer, or pH 8.9 glycine buffer at 37 °C under constant orbital agitation at 150 rpm. Every 24h, the release medium was sampled and replaced with fresh medium to maintain sink conditions. The samples were filtered and stored at 4 °C for OCT determination. The assays were performed in triplicate.

Model fitting was performed using Systat SigmaPlot software analysis with the full 7-day drug release data for each condition. The equations for each tested model are provided in the supplementary material (Table S2).

2.8. 3D-structures antibacterial activity

Antibacterial activity was evaluated against *Staphylococcus aureus* (ATCC 6538) using the agar diffusion method. *S. aureus* cultures were grown in nutrient broth at 37 °C for 24 h. Subsequently, Petri dishes containing Mueller-Hinton agar were inoculated, and 3D prints were placed at the center of each plate. For this assay, smaller-sized 3D prints were used. Each polymer proportion was tested in duplicate. As controls, three formulations (100_{ALG}-0_{CMCh}, 50_{ALG}-50_{CMCh}, and 0_{ALG}-100_{CMCh}) were tested without the addition of OCT to the ink. Inhibition halos were photographed and measured after 24 and 72 h of incubation.

2.9. Statistical analysis

A one-way ANOVA followed by Fisher's LSD test was employed to compare groups. For comparisons involving multiple variables, a two-way ANOVA was applied. The p-values were interpreted as follows: $p < 0.05$ (*), $p < 0.01$ (**), $p < 0.001$ (***), and $p < 0.0001$ (****) were considered statistically significant. Non-significant differences were labelled as "ns".

3. Results and discussion

3.1. 3D-structures printing

In order to produce the 3D prints, printing parameters were adjusted. Even after removing air bubbles from the inks, excessive printing speeds could cause cuts and imperfections. A printing speed of 200 mm/min was determined to be optimal for all prepared inks. Layer height was set at 80 % of the nozzle diameter (0.66 mm) to compensate for ink deformation under its weight. This configuration allowed successful printing of up to 7 layers without compromising layer adhesion. Mesh-like structures were printed at various sizes and with different distances between printer strokes. For most of the assays, square prints measuring a side length of 21.5 mm, consisting of five layers with 2.15 mm spacing between strokes, were printed for each ink. However, to accommodate technical requirements for microbiological assays, smaller square 3D prints measuring 10 mm per side, three layers high, with 1.6 mm stroke spacing were used instead.

3.2. Morphological characterization

3.2.1. Photograps and fidelity studies

GapA was used as a parameter to evaluate the 3D printing fidelity relative to the digital 3D model. As expected, all formulations presented decreases in GapA values after immersion in $CaCl_2$ solution. This phenomenon may result from polymer chain contraction during ionic gelation [44]. A two-way ANOVA revealed that the polymer proportion, calcium immersion, and the interaction between these two factors significantly contributed to the observed variation in the model (27.50 %, 22.35 %, and 17.02 % of the variation, respectively; $p < 0.0001$).

The significance of the differences in GapA before and after calcium treatment is indicated by asterisks in Fig. 3. GapA shrinkage was higher for inks composed of only one type of polymer, with values of 24.6 % for 100_{ALG}-0_{CMCh} and 49.8 % for 0_{ALG}-100_{CMCh} ($p < 0.0001$). The shrinkage for the rest of the inks was 7.4 %, 9.0 %, and 3.9 % for 75_{ALG}-25_{CMCh}, 50_{ALG}-50_{CMCh}, and 25_{ALG}-75_{CMCh}, respectively.

The target GapA by the 3D model was 1.26 mm^2, as shown by the dashed line in Fig. 3. Fidelity to the 3D model can be expressed as the ratio between the expected GapA and the measured GapA in calcium-matured 3D prints. In the present study, the 50_{ALG}-50_{CMCh} polymer proportion presented the best fidelity ratio (Table 1, Fig. 3). In addition, variations in GapA allow the study of the reproducibility of 3D printing. The ALG ink (100_{ALG}-0_{CMCh}) had the lowest standard deviation (Table 1).

3.2.2. Scanning electron microscopy (SEM)

SEM images of the different 3D printing formulations are presented in Fig. 4. The 100 × SEM images show representative segments of the printed materials. The profiles reveal deformations that occur in the hydrogel when it is extruded and then immersed in $CaCl_2$, which were more pronounced in the 0_{ALG}-100_{CMCh} prints; this phenomenon was also evident in the conventional photographs and is reflected in Fig. 3c.

The relative smoothness of the sample surfaces can be observed in Fig. 4. This smoothness was greater in samples containing only alginate, as further confirmed by the standard deviation values obtained from the grayscale histogram of 500 × pictures (Fig. 4, insets).

Salt deposits can be observed in several micrographs (Fig. 4, red arrow). EPMA was performed to characterize these crystals. Despite EPMA offers lower detection limits, it provides a superior spectral resolution, better reproducibility, and more accurate quantitative results than Energy Dispersive X-ray Spectroscopy (EDX). The EPMA spectra showed that they consist primarily of Na and Cl. However, their morphology differs from the typical cubic morphology of NaCl, exhibiting one significantly reduced dimension compared with the other two. Additionally, these structures lack a preferential fracture orientation. The sources of those detected elements could be attributed to sodium originates from sodium alginate, calcium derives from the crosslinking solution, and chloride to residual NaCl from the crosslinking and buffer media.

At higher magnifications, crystalline deposits of much smaller crystals exhibited either cubic or octahedral morphologies with varying degrees of shape and edge definition (Fig. 4, white arrows). Their spectra indicated that their composition is mostly Na and Cl. These two forms are compatible with the cubic crystallography of sodium chloride [45].

The formation of these crystals was attributed to an artifact resulting from the freeze-drying procedure required for SEM sample preparation, and its constituents coming from the contraions from the substances used in the 3D printing ink (i.e. Na coming from ALG) as well as the $CaCl_2$ crosslinking bath.

Due to this crystal formation, grayscale analysis at higher magnification (5000 ×) did not provide reliable information about the porosity of the matrix. However, surfaces exhibiting carbon-rich compositions

Table 1
Alginate and CMCh proportion of the total dry biopolymer. GapA comparison with the 3D model. GapA for 3D model, average GapA, and SD for each 3D print after the calcium chloride bath are shown. Fidelity is defined as the coefficient between GapA for the 3D model and the 3D print.

	Biopolymer dry weight %		Image analysis			
	ALG%	CMCh%	*GapA 3D model (mm^2)*	*GapA AC (mm^2)*	*GapA AC SD (mm^2)*	*Fidelity*
100_{ALG}-0_{CMCh}	100	0	1.26	1.2	0.09	1.05
75_{ALG}-25_{CMCh}	75	25		1.4	0.15	0.9
$50A_{LG}$-50_{CMCh}	50	50		1.25	0.14	1.01
25_{ALG}-75_{CMCh}	25	75		1.18	0.25	1.07
0_{ALG}-100_{CMCh}	0	100		0.69	0.23	1.83

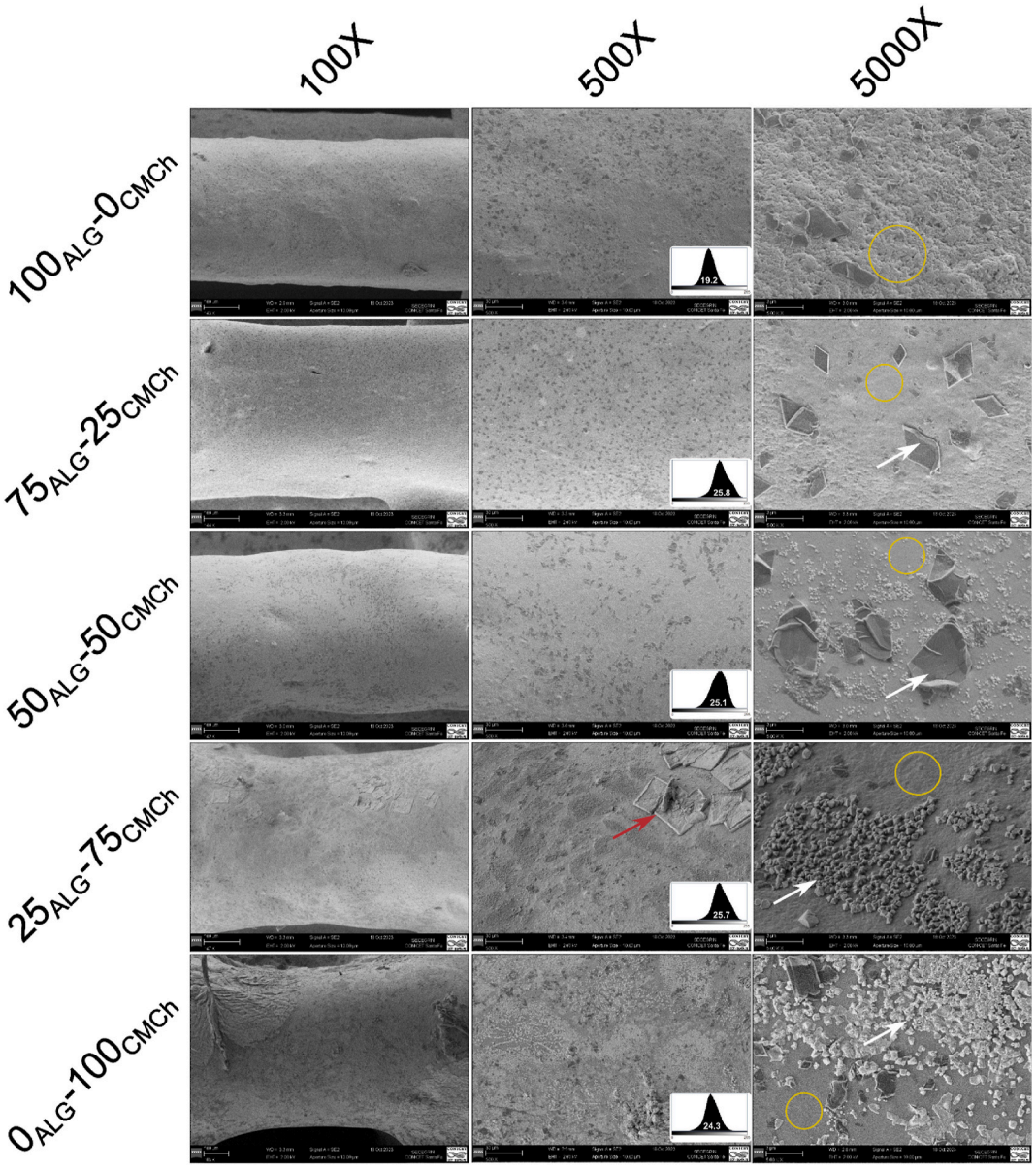

Fig. 4. SEM images obtained from the different 3D prints. Inset in the 500 × images shows the grayscale histogram and its standard deviation. The red arrows indicate crystals rich in Na and Cl. The white arrows indicate smaller crystals rich in Na and Cl, with smaller proportions of Ca. The yellow circles mark the carbon-rich areas of the picture. (For interpretation of the references to colour in this figure legend, the reader is referred to the Web version of this article.)

(Fig. 4, yellow circles) appeared more porous in the 100_{ALG}-0_{CMCh} matrices. Coincidentally, Ca was also found in the polymeric background spectra (Fig. 4, yellow circles), suggesting that Ca was mostly bound to the carboxylic groups and was not expelled from the matrix during the freeze-drying process. In Fig. S1, example EPMA spectra are showed as well as SEM micrograph and its elemental map.

3.3. Chemical interactions studies

3.3.1. Fourier-transform infrared spectroscopy (FTIR)

Fig. 5 shows the FTIR spectra obtained for the pure components and 3D prints. The ALG spectrum displayed a wide peak at approximately 3400 cm^{-1}, which can be attributed to O–H stretching vibrations.

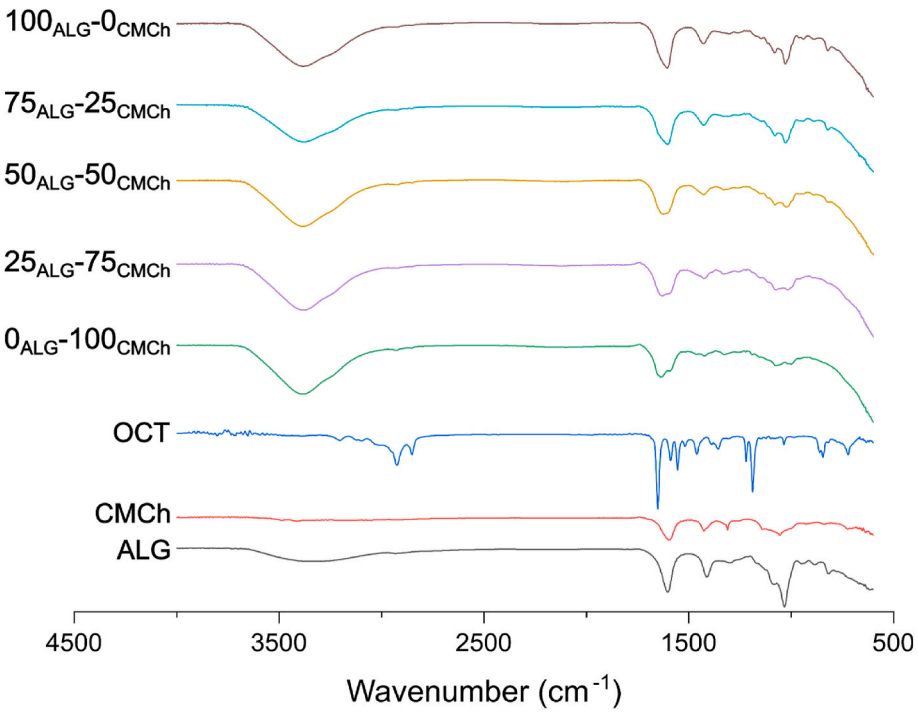

Fig. 5. FTIR spectra for the different 3D prints and their components.

Similarly, the high-intensity wide peak around 3400 cm^{-1} in the 3D-printed spectra can be attributed to O–H stretching from CMCh, ALG, and retained water, as well as N–H stretching from OCT and CMCh [46].

A double peak in the OCT spectrum at 2852.34 cm^{-1} and 2927.55 cm^{-1} can be attributed to alkane C–H stretching in $–CH_3$ and $–CH_2$ groups. The first peak at 723.21 cm^{-1} in the OCT spectrum corresponds to C-Cl stretch, and the peaks at 821.42 and 846.63 cm^{-1} to the C–H bending in the pyridine rings [47]. Sharp peaks at 1189.92 cm^{-1} and 1652.77 cm^{-1} in the same spectrum were attributed to aromatic –C–N– and –C=N– stretches, respectively [48,49].

Sharp peaks at 1411.7 cm^{-1} and 1602.53 cm^{-1} in the ALG spectrum were assigned to the carboxylate $–CO_2^-$ asymmetric and symmetric stretches. Similarly, the CMCh spectrum exhibited analogous peaks at 1596.84 and 1427.13 cm^{-1} [50].

In the 3D prints, peaks corresponding to the asymmetric stretching of the carboxylates in the polymers (1596.84 and 1602.53 cm^{-1}) and the aromatic stretching of –C=N– in OCT (1652.77 cm^{-1}) were observed, along with a complex peak in the region 1550 cm^{-1} to 1700 cm^{-1}. The specific composition of this peak varies depending on the polymer ratio in the print. In the 0_{ALG}-100_{CMCh} print, the peak appears serrated with a maximum at 1637.35 cm-1 and a shoulder at 1592.99 cm^{-1}, representing a bathochromic shift from the two constituent signals. On the other hand, the 100_{ALG}-0_{CMCh} print exhibited a single smooth peak with a maximum at 1604.56 cm^{-1} and a barely perceptible shoulder at approximately 1650 cm^{-1}. This represents a hypsochromic shift from the peak originally at 1602.5 cm^{-1}. The prints in which the matrix was composed of different proportions of the polymer presented intermediate profiles to those presented in the 0_{ALG}-100_{CMCh} and 100_{ALG}-0_{CMCh} prints in that area of the spectrum. A supplementary figure is provided with details of these areas of the spectra (Fig. S2).

These findings suggest an interaction between the CMCh and ALG polymers and the drug, particularly in the carboxylic groups of the polymers and the aromatic nitrogens in OCT. In addition, it is interesting to note the intricate molecular composition of polymers and antibiotics, which can lead to interactions and phenomena that are challenging to isolate and fully elucidate [51].

3.3.2. *Thermogravimetric analysis (TGA)*

TGA is a common analysis for polymeric materials. It allows for estimation of the interactions in the material, its water content, and the effects of adding crosslinkers or fillers. Fig. 6 shows the TGA results of this study.

Three thermogravimetric effects are observed in ALG thermograms. The initial slope before 200 °C and mass loss of 10 % were assigned to dehydration. The second process is a weight loss of 35 % and a derivative peak at 236.5 °C (Fig. 6). This phenomenon is typically associated with the fragmentation of ALG chains due to the breakage of glycosidic bonds [52]. After 260 °C to the end of the TGA run, the final long slope exhibited a weight loss of 16 %. This result can be explained by the pyrolytic decomposition of ALG residues and short chains into Na_2CO_3. The final residue for this sample was 39,5 % of the initial weight.

Analogously to ALG, CMCh presents three distinct thermogravimetric effects: 1) a weight loss of 9 % until 240 °C, assigned to dehydration; 2) a pronounced weight loss of 26 % of the initial mass with a derivative peak at 268.5 °C, related to the fragmentation of the chains, and 3) a process from 300 to 600 °C, attributed to pyrolysis of the monomers [53]. The final residue was 46 % of the initial weight.

The OCT thermogram showed one-step pyrolysis at 249–338 °C (derivative peak at 317.5 °C), to a residue of 1.9 %. This behavior is consistent with the results for a pure organic non-polymeric substance.

When the inks were prepared using one of the polymers, the T_{max} of the first degradation process increased for ALG (from 236.7 to 251.7 °C) and CMCh (from 268.6 to 274 °C) compared with the pure respective biopolymers, indicating that the small amount of calcium added during ink preparation indeed increased thermal stability. The further inclusion of calcium into the structure after printing affected ALG and CMCh differently. In 100_{ALG}-0_{CMCh} prints, we observed an even more pronounced increase in main pyrolysis (to 281 °C). On the other hand, the 0_{ALG}-100_{CMCh} thermogram presents several peaks between 200 °C and 400 °C. These different degradation processes can originate from the higher molecular inhomogeneities of CMCh compared with ALG. Additionally, in samples where this maturation in calcium chloride solution was applied, an additional thermal degradation can be observed after 500 °C; this last process was assigned to a further calcination of the

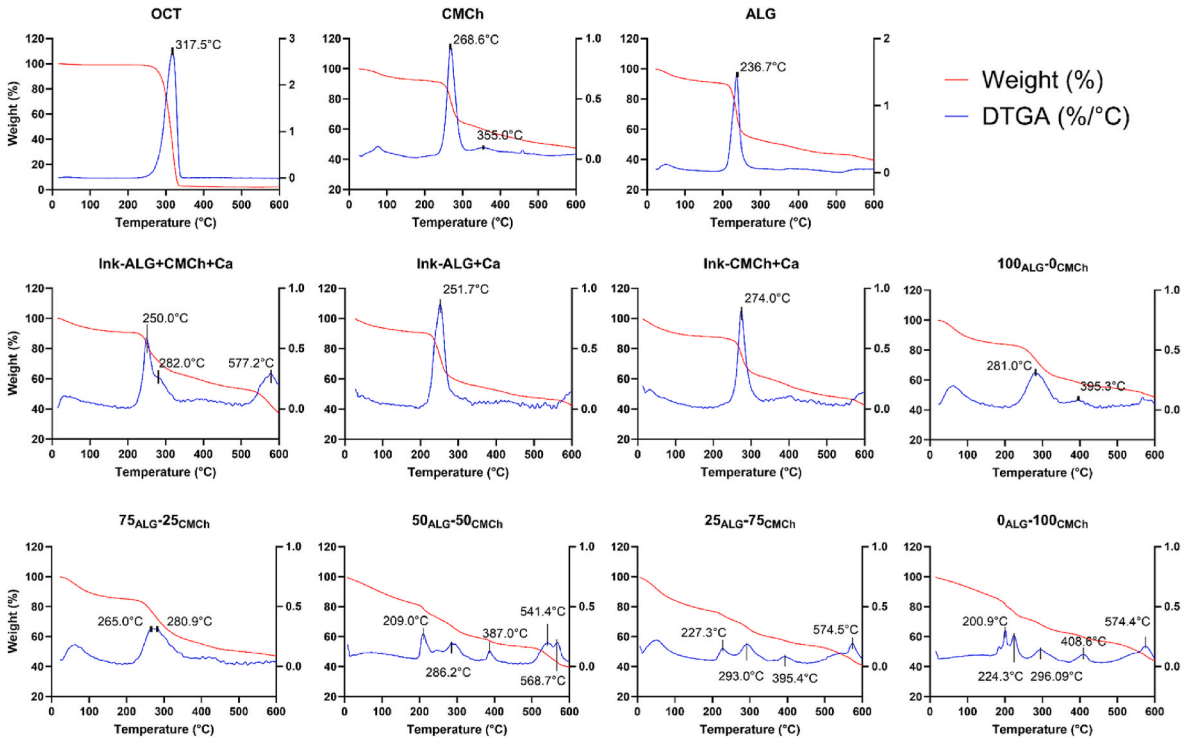

Fig. 6. Thermograms (weight% % vs. temperature, red line left axis) and DTGA (derivative of weight% vs temperature, blue line right axis) of each component used and the 3D prints obtained. (For interpretation of the references to colour in this figure legend, the reader is referred to the Web version of this article.)

calcium compounds formed in the previous step [54].

In summary, immersion in a calcium chloride solution generates complex thermograms that indicate the appearance of new interactions in the materials, both with calcium and between polymers.

3.4. Swelling studies

Swelling behavior provides insight into how the components of a formulation affect their interactions with a specific aqueous medium. To evaluate the effect of pH on 3D prints, non-calcium-chelating buffers

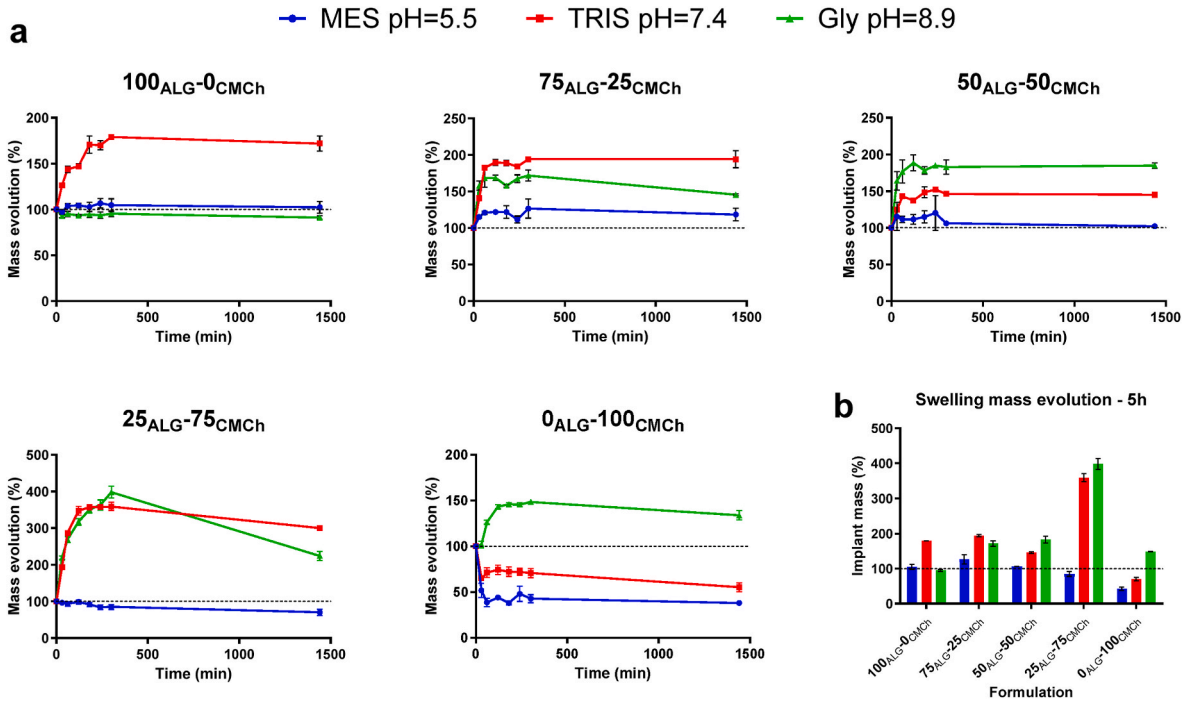

Fig. 7. Swelling behavior of the 3D-printed alginate/CMCh constructs loaded with OCT under physiological conditions. Swelling profiles up to 24 h and 3D print mass measurements after 5 h. (a) Swelling profiles of the 3D prints during immersion in different non-chelating buffer solutions (pH 5.5, 7.4 and 8.9) at 37 °C over a 24-h period. Data are presented as percentage weight change relative to the initial dry mass (mean ± SD, n = 3). (B) Residual mass of the 3D prints after 5 h of immersion in the same buffer systems, illustrating differences in stability and water uptake depending on polymer composition and pH environment.

were used in order to preserve the structural morphology and composition. Fig. 7a shows the swelling results for the different 3D printings.

The 3D prints submerged in the MES buffer showed a small or no weight increase. For 3D prints containing varying amounts of ALG, this is consistent with the well-documented pH-dependent swelling behavior [55,56]. On the other hand, in the particular case of 0_{ALG}-100_{CMCh} 3D prints, the weight decreased. This can be explained by the fact that, at this pH, CMCh is near its isoelectric point (pI~5), which can cause shrinkage and consequent water expulsion from the hydrogel [57].

In general, the addition of CMCh reduced weight gain in 3D prints at pH 7.4. Prints without ALG (0_{ALG}-100_{CMCh}) lost weight. An exception to this trend was observed in 25_{ALG}-75_{CMCh} prints. Initially, these prints gained nearly four times their original mass. However, after the first hydration phase, they underwent a dissolution process, as evidenced by subsequent weight loss.

At high pH (Gly = 8.9), it would be expected that ALG-based 3D prints would swell even more than at pH 7.4, due to increased deprotonation of carboxylic groups and the resulting electrostatic repulsion between chains [56]. However, this was not observed under the tested conditions. Instead, the 100_{ALG}-0_{CMCh} 3D prints showed no swelling. A possible explanation for this involves the ionic state of OCT. At high pH, OCT's ionization equilibrium shifts toward a more hydrophobic, uncharged species, thereby inhibiting hydration. This phenomenon was reduced as the proportion of CMCh increased in the 3D prints. Again, the anomalous behavior of 25_{ALG}-75_{CMCh} 3D prints presented a swelling much higher than the rest of the formulations with any other proportion (Fig. 7b). This suggests that a small proportion of ALG generates heterogeneities or interactions in the polymer matrix that are not observed in prints either without ALG or with higher ALG proportions.

3.5. OCT release from the 3D prints

The amount of OCT in the wash water and calcium chloride bath was found to be below the limit of quantification of the method used. Therefore, the encapsulation efficiency for all 3D prints was greater than 99.9 %. As a result, the initial mass of OCT was used to normalize the release profiles. Considering this, Fig. 8 shows the OCT release profiles obtained for the different buffers used.

Drug release in MES buffer (Fig. 8a, blue lines) was highly dependent on the CMCh proportion in the 3D print, and OCT release could not be explained by the swelling effect alone. At this pH, ALG was already ionized (pKa = 3.3–3.6); therefore, interaction with OCT was expected. However, CMCh was taking on a zwitterionic form (pI ~5.2), and no ionic interaction was expected to retain OCT in the matrix in the 0_{ALG}-100_{CMCh} prints. Consequently, no enhanced OCT release was observed in 100_{ALG}-0_{CMCh} due to the absence of CMCh. Furthermore, the mixture-based 3D prints presented intermediate release profiles. However, in 50–50 prints, OCT release was faster in MES than in TRIS at short times (before 2h). Interestingly, in 25_{ALG}-75_{CMCh} prints, OCT release was even higher than in full CMCh prints (0_{ALG}-100_{CMCh}), but they did not show significant differences in MES (Fig. 8b).

At pH 7.4, OCT release (Fig. 8a, red lines) from 3D prints was slower in prints with higher CMCh content. However, after 7 days of release, these differences were no longer evident, with all but the 100_{ALG}-0_{CMCh} prints releasing more than 60 % of the drug ($p < 0.05$).

At pH 8.9 (Fig. 8a, green lines), slow release was observed regardless of the 3D print composition. This can be easily explained by the low solubility of OCT resulting from the loss of its ionic charge. However, only CMCh 3D prints exhibited significantly higher ($p > 0.05$) release after 7 days.

Of the five models tested to fit the release profiles, the semi-empirical Korsmeyer-Peppas model was the best fit for all polymeric proportions and pH conditions (Table 2). In this model, the exponent "n" could indicate the release mechanism from the matrix; a perfectly cylindrical matrix with only diffusion as the release mechanism should fit n = 0.45. For the matrices covered in this study, cylinders are a good model, since the 3D prints can be considered as multiple layers of intersected cylinders, and the adjusted parameter "n" was well below 0.45 in all cases, suggesting Fickian diffusion of the drug was hindered by either physical or molecular interactions [58,59].

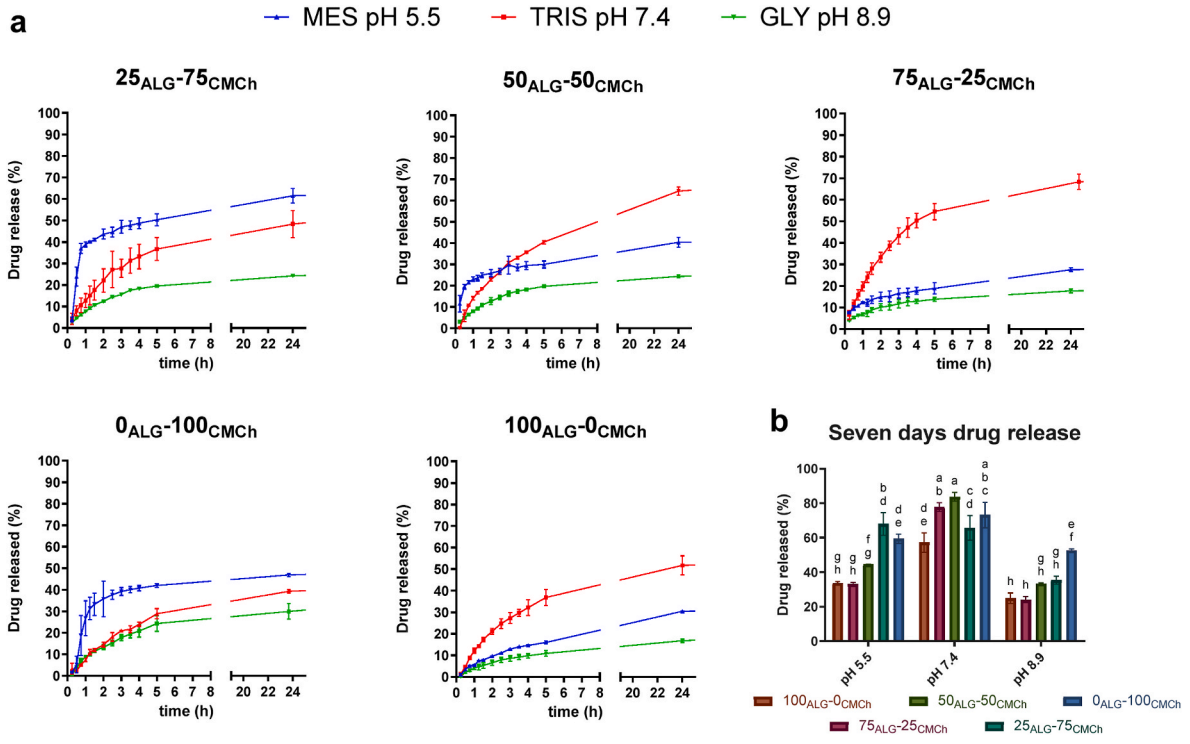

Fig. 8. Release profiles from 3D prints in three buffers, MES pH = 5.5 (a, blue line), TRIS pH = 7.4 (b, red line), and Glycine buffer pH = 8.9 (c, green line). OCT mass released from the 3D prints after 7 days (b, bars graph) submerged in MES (pH = 5.5), TRIS (pH = 7.4), or Gly (pH = 8.9) buffer. Letters represent groups without statistical differences ($p > 0.05$). (For interpretation of the references to colour in this figure legend, the reader is referred to the Web version of this article.)

Table 2
Parameters obtained for Korsmeyer-Peppas fits for each release profile.

		Korsmeyer-Peppas parameters	
3D print	Buffer	n	k
100_{ALG}-0_{CMCh}	MES	0.24	9.49
	TRIS	0.21	19.37
	Gly	0.25	6.26
75_{ALG}-25_{CMCh}	MES	0.17	13.36
	TRIS	0.19	30.08
	Gly	0.18	8.75
50_{ALG}-50_{CMCh}	MES	0.14	23.20
	TRIS	0.28	21.07
	Gly	0.22	10.90
25_{ALG}-75_{CMCh}	MES	0.11	37.20
	TRIS	0.24	19.68
	Gly	0.23	10.69
0_{ALG}-100_{CMCh}	MES	0.18	27.51
	TRIS	0.30	13.69
	Gly	0.26	13.20

Overall, drug release profiles were highly dependent on pH and polymeric composition. The phenomena governing this pH dependence are several. The effect of ionic charge of the matrix, particularly carboxyl groups, on OCT release has been reported, which could explain both the dependence of release on polymer composition and the OCT hindered diffusion phenomena suggested by the fitting [60]. This, coupled with pH-dependent swelling of the 3D prints, can produce complex pH-dependent behaviors. These results allow for the possibility of tuning the biopolymeric composition of the inks for different wound situations. However, some unexpected phenomena can occur due to the material's complexity, as observed in the 25_{ALG}-75_{CMCh} 3D prints. The components may undergo microphase separation, which can create regions with different swelling capacities. This can lead to a localized composition with different polymer composition gradients and unexpected swelling/release patterns [61,62]. The results showed that 3D printing requires careful selection of biomaterials and mixture composition in order to achieve predictable release patterns.

To the best of our knowledge, the literature shows only one report on the use of biopolymer-based 3D prints for OCT delivery for wound treatment. Niziol et al. (2021) studied the combination of synthetic polymers with ALG to obtain printable inks [41]. Mechanistically, these 3D prints showed a release highly dependent on temperature while submerged in PBS. This buffer can chelate calcium cations, inducing ion exchange with consequent distortion of the polymeric matrix and this loss of integrity induced OCT release. At 30 °C, the authors reported that 100 % of OCT was released after 25 h of assay. However, this study did not explore different pH conditions and buffer types. Our study focused on the mechanism of controlled release in response to pH, which arises from the ionic equilibrium between OCT, alginate and CMCh (Fig. 1). This interplay controlled swelling behavior at different pH values: acidic conditions promote stronger ionic crosslinking and slower release, whereas alkaline conditions weaken interactions and accelerate drug diffusion. This pH-dependent mechanism distinguishes our formulation from previously published systems, which were primarily focused on synthetic polymers or nanoparticle incorporation. Our study also investigated different buffers that avoid cation chelation. This approach enabled us to specifically study the pH dependence of the matrix, demonstrating enhanced OCT release at the wound pH (7.4) compared with healthy skin pH (~5) [9,11]. In addition, all tested 3D prints released less than 80 % of OCT after 7 days of assay, which demonstrated improved release control capacities of the designed formulations.

3.6. Antimicrobial activity

All tested formulations containing OCT showed inhibition halos at 24 h, as shown in Fig. 9. On the other hand, no inhibition halos were detected in plates treated with OCT-free 3D prints (Fig. S3). In addition, bacterial growth could be observed on these prints. Although some studies suggest that CMCh possesses intrinsic antibacterial activity against *S. aureus* [63], our results indicated that the observed antimicrobial activity originates exclusively from OCT rather than from other components. Moreover, the results showed that OCT retained its antimicrobial activity after the preparation, extrusion, and maturation of the 3D prints. After 72 h, some aging was observable in the 3D prints, evident through yellowing and drying, but still the inhibition halos

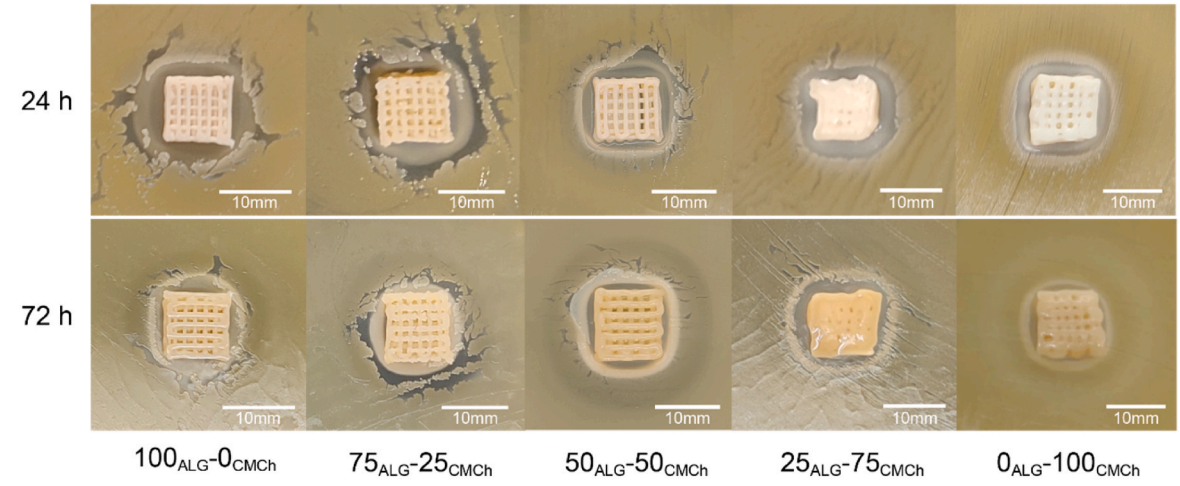

	100-0	75-25	50-50	25-75	0-100
24h	13.3±1.4	14.0±0.9	15.7±0.6	13.7±0.5	15.2±0.9
72h	13.3±1.0	14.3±0.8	14.7±0.9	13.4±0.6	14.9±0.8

All measurements are expressed in millimeters.

Fig. 9. Inhibition halos produced by 3D prints after 24 h and 72 h in solid *S. aureus* cultures. The inhibition zone diameters were measured from the pictures 6 times per replicate and reported in millimeters (mean ± SD, n = 2). Statistical analysis revealed no significant differences between the inhibition halos.

remained in the same values than those observed after 24 h (**Table in** Fig. 9). Despite the different compositions and *in vitro* swelling/release patterns, the microbiological results demonstrated the ability of these 3D-printed systems to produce localized inhibition halos through active OCT release.

4. Conclusions

Complex wounds remain a major clinical challenge, and current approaches often rely on the smart release of antiseptic drugs. Hydrogels have been extensively investigated as wound dressings since they not only isolate the wound from the environment but also provide a moist environment while absorbing excess water from exudates [9]. In this regard, biopolymer-based hydrogels are particularly attractive as wound dressing materials due to their biocompatibility, high permeability, high water absorption capacity, and responsiveness to physiological stimuli such as temperature and pH [64,65].

With the emergence of personalized medicine, 3D printing has become a viable alternative for wound treatment, allowing adjustments based on the wound type, metabolic state, and therapeutic needs of the patient. In these cases, 3D printing can modify not only the geometry of the wound dressing but also its porosity and thickness, even adapting to computerized models of wounds [16]. In this study, extrusion-based 3D printing inks were successfully produced using biopolymers such as alginate and CMCh in five different ratios, and mesh-like 3D prints were fabricated. The extrusion-based 3D printing was selected for preparation, since it is especially advantageous for wound-healing applications, as it allows the incorporation of sensitive antimicrobial agents and biopolymers while preserving their structural and biological functionality.

The 3D prints were physicochemical characterized. The molecular interactions between the ink components were demonstrated using FTIR and were evidenced in the thermograms. While chemical and physicochemical interactions within a polymeric matrix loaded with an active pharmaceutical ingredient are indispensable to explain the material's macroscopic properties, inhomogeneities at the molecular level and the multiplicity of interactions in systems of three or more components complicate this analysis and, consequently, make their properties difficult to predict [12,66]. Therefore, swelling and OCT release profiles cannot be explained except from multiple perspectives, including but not limited to polymer solubility, drug solubility, electrostatic interactions, and the effect of pH on all these factors.

Sustained drug release enables the maintenance of an adequate concentration of the active agent over time, thereby reducing the frequency of interventions or doses and improving patient compliance and the clinical efficacy of the treatment [12,16].

Previously, Niziol et al. developed a high-fidelity 3D printing method, but in pursuit of thermoresponsiveness [41]. In this study, we aimed to develop biopolymer-based 3D prints with pH-dependent drug release. The hydration and release profiles of OCT from these 3D prints showed complex pH behavior that, as stated, cannot be easily predicted from the characteristics of their components and points to multiple interactions between them. OCT itself does not act as a passive molecule in these interactions; however, its charge and that of its environment affect the release profiles, as previously demonstrated by Maraldi et al. [60].

However, OCT was incorporated into the polymeric matrices tested in this study with a high degree of encapsulation. The developed system delivered OCT locally for 7 days in a pH-controlled manner, enhancing its release at near-neutral pH (typical of wounds) while reducing its release at slightly acidic pH (characteristic of healing wounds or healthy skin). This reduces the possible adverse effects associated with the active components in tissues where they are not needed. The polymer ratio can be selected based on the drug release, pH, and hydration requirements of the target.

S. aureus, one of the most prevalent pathogens in chronic wounds and burns due to its opportunistic nature, contributes to delayed healing and may ultimately lead to systemic complications [67]. The effectiveness of the encapsulated active ingredient in the 3D prints was demonstrated in agar diffusion assays against *S. aureus* for up to 72 h, with no observed effect from the intrinsic activity of the biopolymer matrix.

In conclusion, this study demonstrates that 3D printing of OCT-loaded biopolymeric matrices is a promising strategy for addressing the health problems associated with chronic and acute wounds. To the best of our knowledge, the first report of a fully biopolymeric, pH-sensitive system incorporating OCT, fabricated via extrusion-based 3D printing. This approach enables tunable swelling and controlled antibiotic release without the need for synthetic polymers or additives, which distinguishes it from previous works. The versatility of 3D printing further offers the potential to customize treatments according to each patient's specific needs.

CRediT authorship contribution statement

Ignacio Rivero Berti: Writing – review & editing, Writing – original draft, Software, Methodology, Investigation, Formal analysis, Data curation, Conceptualization. **Manuel Horue:** Writing – original draft, Formal analysis, Data curation, Conceptualization. **Tugce Boztepe:** Writing – original draft, Formal analysis, Data curation, Conceptualization. **Marcelo Calderón:** Writing – review & editing, Resources, Formal analysis, Conceptualization. **Luciano Mengatto:** Writing – review & editing, Formal analysis, Conceptualization. **Stephan Gehring:** Writing – review & editing, Resources, Formal analysis, Conceptualization. **Sergio Katz:** Validation, Software, Methodology, Formal analysis, Data curation. **Germán Islan:** Writing – review & editing, Writing – original draft, Supervision, Project administration, Funding acquisition, Formal analysis, Conceptualization. **Federico Karp:** Writing – review & editing, Writing – original draft, Supervision, Project administration, Methodology, Formal analysis, Data curation, Conceptualization.

Declaration of competing interest

The authors declare that they have no known competing financial interests or personal relationships that could have appeared to influence the work reported in this paper.

Acknowledgment

This work was partially supported by UNLP (PPID X077) and CONICET (PIP 2051, PIBAA 1078, PUE 0010).

Appendix A. Supplementary data

Supplementary data to this article can be found online at https://doi.org/10.1016/j.jddst.2025.107558.

Data availability

Data will be made available on request.

References

[1] E.M. Tottoli, R. Dorati, I. Genta, E. Chiesa, S. Pisani, B. Conti, Skin wound healing process and new emerging technologies for skin wound care and regeneration, Pharmaceutics 12 (8) (Aug. 2020) 735, https://doi.org/10.3390/pharmaceutics12080735.

[2] S.K. Han, Innovations and Advances in Wound Healing, Springer Nature, Singapore, 2023 [Online]. Available: https://books.google.com.ar/books?id=8Re2EAAAQBAJ.

[3] J. Dissemond, A. Bültemann, V. Gerber, B. Jäger, K. Kröger, C. Münter, Diagnosis and treatment of chronic wounds: current standards of Germany's Initiative for Chronic Wounds e. V, J. Wound Care 26 (12) (Dec. 2017) 727–732, https://doi.org/10.12968/jowc.2017.26.12.727.

[4] V. Falanga, et al., Chronic wounds, Nat. Rev. Dis. Primers 8 (1) (July 2022) 1–21, https://doi.org/10.1038/s41572-022-00377-3.

[5] H.S. Kim, X. Sun, J.-H. Lee, H.-W. Kim, X. Fu, K.W. Leong, Advanced drug delivery systems and artificial skin grafts for skin wound healing, Adv. Drug Deliv. Rev. 146 (June 2019) 209–239, https://doi.org/10.1016/j.addr.2018.12.014.
[6] 'Acute Wound Care Market Size to Hit USD 14.27 Billion by, 2025. https://www.precedenceresearch.com/acute-wound-care-market. (Accessed 26 May 2025).
[7] 'Chronic Wound Care Market Size, Share | Global Report, 2025. https://www.fortunebusinessinsights.com/industry-reports/chronic-wound-care-market-100222. (Accessed 26 May 2025).
[8] D.T. Uchida, M.L. Bruschi, 3D printing as a technological strategy for the personalized treatment of wound healing, AAPS PharmSciTech 24 (1) (Jan. 2023) 41, https://doi.org/10.1208/s12249-023-02503-0.
[9] Y. Liang, J. He, B. Guo, Functional hydrogels as wound dressing to enhance wound healing, ACS Nano 15 (8) (Aug. 2021) 12687–12722, https://doi.org/10.1021/acsnano.1c04206.
[10] R. Tiwari, K. Pathak, Local drug delivery strategies towards wound healing, Pharmaceutics 15 (2) (Feb. 2023) 634, https://doi.org/10.3390/pharmaceutics15020634.
[11] P. Sim, X.L. Strudwick, Y. Song, A.J. Cowin, S. Garg, Influence of acidic pH on wound healing in vivo: a novel perspective for wound treatment, Int. J. Mol. Sci. 23 (21) (Nov. 2022) 13655, https://doi.org/10.3390/ijms232113655.
[12] P. Lu, et al., Harnessing the potential of hydrogels for advanced therapeutic applications: current achievements and future directions, Sig Transduct Target Ther 9 (1) (July 2024) 1–66, https://doi.org/10.1038/s41392-024-01852-x.
[13] A.G. Tabriz, D. Douroumis, Recent advances in 3D printing for wound healing: a systematic review, J. Drug Deliv. Sci. Technol. 74 (Aug. 2022) 103564, https://doi.org/10.1016/j.jddst.2022.103564.
[14] M. Alizadehgiashi, et al., Multifunctional 3D-printed wound dressings, ACS Nano 15 (7) (July 2021) 12375–12387, https://doi.org/10.1021/acsnano.1c04499.
[15] I. Rivero Berti, et al., Enzymatic active release of violacein present in nanostructured lipid carrier by lipase encapsulated in 3D-bioprinted chitosan-hydroxypropyl methylcellulose matrix with anticancer activity, Front. Chem. 10 (July 2022) 756, https://doi.org/10.3389/fchem.2022.914126.
[16] M. Deptuła, M. Zawrzykraj, J. Sawicka, A. Banach-Kopeć, R. Tylingo, M. Pikuła, Application of 3D- printed hydrogels in wound healing and regenerative medicine, Biomed. Pharmacother. 167 (Nov. 2023) 115416, https://doi.org/10.1016/j.biopha.2023.115416.
[17] Y. Zheng, et al., Melt extrusion deposition (MED^{TM}) 3D printing technology – a paradigm shift in design and development of modified release drug products, Int. J. Pharm. 602 (June 2021) 120639, https://doi.org/10.1016/j.ijpharm.2021.120639.
[18] Triastek's 3D Printed Gastric Retention Product T22 Receives FDA Clearance of IND Application', BioSpace. Accessed: April. 15, 2025. [Online]. Available: https://www.biospace.com/triastek-s-3d-printed-gastric-retention-product-t22-receives-fda-clearance-of-ind-application.
[19] Y. Zhou, et al., A Novel oral 3D-printed delayed- and extended-release Tofacitinib (T19) for the treatment of Rheumatoid Arthritis and related inflammatory Diseases, in: ACR Meeting Abstracts, Nov. 2024 [Online]. Available: https://acrabstracts.org/abstract/a-novel-oral-3d-printed-delayed-and-extended-release-tofacitinib-t19-for-the-treatment-of-rheumatoid-arthritis-and-related-inflammatory-diseases/. (Accessed 15 April 2025).
[20] I. Matai, G. Kaur, A. Seyedsalehi, A. McClinton, C.T. Laurencin, Progress in 3D bioprinting technology for tissue/organ regenerative engineering, Biomaterials 226 (Jan. 2020) 119536, https://doi.org/10.1016/j.biomaterials.2019.119536.
[21] U. Vegad, M. Patel, D. Khunt, O. Zupančič, S. Chauhan, A. Paudel, pH stimuli-responsive hydrogels from non-cellulosic biopolymers for drug delivery, Front. Bioeng. Biotechnol. 11 (2023) Sept, https://doi.org/10.3389/fbioe.2023.1270364.
[22] F. Fayyazbakhsh, M.J. Khayat, M.C. Leu, 3D-Printed gelatin-alginate hydrogel dressings for burn wound healing: a Comprehensive study, Int J Bioprint 8 (4) (2022) 618, https://doi.org/10.18063/ijb.v8i4.618.
[23] C.M. Cleetus, et al., Alginate hydrogels with Embedded ZnO nanoparticles for wound healing Therapy, Int. J. Nanomed. 15 (2020) 5097–5111, https://doi.org/10.2147/IJN.S255937.
[24] T. Huang, Z. Sun, D.E. Heath, N. O'Brien-Simpson, A.J. O'Connor, 3D printed and smart alginate wound dressings with pH-responsive drug and nanoparticle release, Chem. Eng. J. 492 (July 2024) 152117, https://doi.org/10.1016/j.cej.2024.152117.
[25] D. Wang, N. Zhang, G. Meng, J. He, F. Wu, The effect of form of carboxymethyl-chitosan dressings on biological properties in wound healing, Colloids Surf. B Biointerfaces 194 (Oct. 2020) 111191, https://doi.org/10.1016/j.colsurfb.2020.111191.
[26] E. Naseri, C. Cartmell, M. Saab, R.G. Kerr, A. Ahmadi, Development of N,O-carboxymethyl chitosan-starch biomaterial inks for 3D printed wound dressing applications, Macromol. Biosci. 21 (12) (2021) 2100368, https://doi.org/10.1002/mabi.202100368.
[27] L. García, et al., Ionically-crosslinked carboxymethyl chitosan scaffolds by additive manufacturing for antimicrobial wound dressing applications, Carbohydr. Polym. 346 (Dec. 2024) 122640, https://doi.org/10.1016/j.carbpol.2024.122640.
[28] N. Kim, et al., 3D-Printed functional hydrogel by DNA-induced biomineralization for accelerated diabetic wound healing (Adv. Sci. 17/2023, Adv. Sci. (Weinh.) 10 (17) (June 2023) 2370104, https://doi.org/10.1002/advs.202370104.
[29] F. Tsegay, M. Hisham, M. Elsherif, A. Schiffer, H. Butt, 3D printing of pH indicator auxetic hydrogel skin wound dressing, Molecules 28 (3) (Jan. 2023) 1339, https://doi.org/10.3390/molecules28031339.
[30] C. Bergonzi, A. Bianchera, G. Remaggi, M.C. Ossiprandi, R. Bettini, L. Elviri, 3D printed chitosan/alginate hydrogels for the controlled release of silver sulfadiazine in wound healing applications: design, characterization and antimicrobial activity, Micromachines 14 (1) (Jan. 2023) 137, https://doi.org/10.3390/mi14010137.
[31] T. Huang, Z. Sun, D.E. Heath, N. O'Brien-Simpson, A.J. O'Connor, 3D printed and smart alginate wound dressings with pH-responsive drug and nanoparticle release, Chem. Eng. J. 492 (July 2024) 152117, https://doi.org/10.1016/j.cej.2024.152117.
[32] M. Rzycki, D. Drabik, K. Szostak-Paluch, B. Hanus-Lorenz, S. Kraszewski, Unraveling the mechanism of octenidine and chlorhexidine on membranes: does electrostatics matter? Biophys. J. 120 (16) (Aug. 2021) 3392–3408, https://doi.org/10.1016/j.bpj.2021.06.027.
[33] C. Wiegand, M. Abel, P. Ruth, P. Elsner, U.-C. Hipler, pH influence on antibacterial efficacy of common antiseptic substances, Skin Pharmacol. Physiol. 28 (3) (Jan. 2015) 147–158, https://doi.org/10.1159/000367632.
[34] N. Malanovic, A. Ön, G. Pabst, A. Zellner, K. Lohner, Octenidine: novel insights into the detailed killing mechanism of Gram-negative bacteria at a cellular and molecular level, Int. J. Antimicrob. Agents 56 (5) (Nov. 2020) 106146, https://doi.org/10.1016/j.ijantimicag.2020.106146.
[35] G. Hämmerle, R. Strohal, Efficacy and cost-effectiveness of octenidine wound gel in the treatment of chronic venous leg ulcers in comparison to modern wound dressings, Int. Wound J. 13 (2) (Mar. 2014) 182–188, https://doi.org/10.1111/iwj.12250.
[36] Use of octenidine dihydrochloride in managing chronic wounds: a case series – wounds Asia. https://woundsasia.com/journal-articles/use-of-octenidine-dihydrochloride-in-managing-chronic-wounds-a-case-series/. (Accessed 5 March 2025).
[37] S. Seiser, et al., Octenidine-based hydrogel shows anti-inflammatory and protease-inhibitory capacities in wounded human skin, Sci. Rep. 11 (1) (Jan. 2021) 32, https://doi.org/10.1038/s41598-020-79378-9.
[38] V. Chiaula, J. Jeppe Madsen, F.B. Madsen, P. Mazurek, A.C. Nielsen, A.L. Skov, 'Antimicrobial silicone skin adhesives facilitated by controlled octenidine release from glycerol compartments', Int. J. Soc. Netw. Min. 14 (3) (July 2023) 369–389, https://doi.org/10.1080/19475411.2023.2240743.
[39] Y. Alkhatib, M. Dewaldt, S. Moritz, R. Nitzsche, D. Kralisch, D. Fischer, Controlled extended octenidine release from a bacterial nanocellulose/Poloxamer hybrid system, Eur. J. Pharm. Biopharm. 112 (Mar. 2017) 164–176, https://doi.org/10.1016/j.ejpb.2016.11.025.
[40] D. Ciecholewska-Juśko, A. Junka, K. Fijałkowski, The cross-linked bacterial cellulose impregnated with octenidine dihydrochloride-based antiseptic as an antibacterial dressing material for highly-exuding, infected wounds, Microbiol. Res. 263 (Oct. 2022) 127125, https://doi.org/10.1016/j.micres.2022.127125.
[41] M. Nizioł, J. Paleczny, A. Junka, A. Shavandi, A. Dawiec-Liśniewska, D. Podstawczyk, 3D printing of thermoresponsive hydrogel laden with an antimicrobial agent towards wound healing applications, Bioengineering 8 (6) (June 2021), https://doi.org/10.3390/bioengineering8060079.
[42] J. Schindelin, et al., Fiji: an open-source platform for biological-image analysis, Nat. Methods 9 (7) (July 2012) 676–682, https://doi.org/10.1038/nmeth.2019.
[43] G.A. Islan, M.L. Cacicedo, V.E. Bosio, G.R. Castro, Development and characterization of new enzymatic modified hybrid calcium carbonate microparticles to obtain nano-architectured surfaces for enhanced drug loading, J. Colloid Interface Sci. 439 (2015) 76–87, https://doi.org/10.1016/j.jcis.2014.10.007.
[44] C. Bennacef, S. Desobry, J. Jasniewski, S. Leclerc, L. Probst, S. Desobry-Banon, Influence of alginate properties and calcium chloride concentration on alginate bead reticulation and size: a phenomenological approach, Polymers 15 (20) (Oct. 2023) 4163, https://doi.org/10.3390/polym15204163.
[45] A. Jain, et al., Commentary: the Materials Project: a materials genome approach to accelerating materials innovation, APL Mater. 1 (1) (July 2013) 011002, https://doi.org/10.1063/1.4812323.
[46] I.M. El-Sherbiny, Synthesis, characterization and metal uptake capacity of a new carboxymethyl chitosan derivative, Eur. Polym. J. 45 (1) (Jan. 2009) 199–210, https://doi.org/10.1016/j.eurpolymj.2008.10.042.
[47] I. Ibrahim, S. Yunus, A. Hashim, Relative performance of isopropylamine, pyrrole and pyridine as corrosion Inhibitors for carbon steels in Saline water at mildly elevated temperatures, Int. J. Sci. Eng. Res. 4 (Mar. 2013).
[48] F. Pan, et al., Bioresponsive hybrid nanofibers enable controlled drug delivery through glass transition switching at physiological temperature, ACS Appl. Bio Mater. 4 (5) (May 2021) 4271–4279, https://doi.org/10.1021/acsabm.1c00099.
[49] M. Pandian, V.A. Kumar, R. Jayakumar, Antiseptic chitosan bandage for preventing topical skin infections, Int. J. Biol. Macromol. 193 (Dec. 2021) 1653–1658, https://doi.org/10.1016/j.ijbiomac.2021.11.002.
[50] M. Kurniasih, T. Cahyati Purwati, R.S. Dewi, Carboxymethyl chitosan as an antifungal agent on gauze, Int. J. Biol. Macromol. 119 (Nov. 2018) 166–171, https://doi.org/10.1016/j.ijbiomac.2018.07.038.
[51] F. Karp, L.N. Turino, I.M. Helbling, G.A. Islan, J.A. Luna, D.A. Estenoz, In situ formed implants, based on PLGA and eudragit blends, for novel florfenicol controlled release formulations, J. Pharmaceut. Sci. 110 (3) (Mar. 2021) 1270–1278, https://doi.org/10.1016/j.xphs.2020.11.006.
[52] C.G. Flores-Hernández, M. de los A. Cornejo-Villegas, A. Moreno-Martell, A. Del Real, Synthesis of a biodegradable polymer of poly (sodium alginate/ethyl acrylate), Polymers 13 (4) (Jan. 2021), https://doi.org/10.3390/polym13040504, 4.
[53] H.E. Salama, M.S. Abdel Aziz, Novel biocompatible and antimicrobial supramolecular *O*-carboxymethyl chitosan biguanidine/zinc physical hydrogels, Int. J. Biol. Macromol. 163 (Nov. 2020) 649–656, https://doi.org/10.1016/j.ijbiomac.2020.07.029.

[54] J. Zhang, Q. Ji, X. Shen, Y. Xia, L. Tan, Q. Kong, Pyrolysis products and thermal degradation mechanism of intrinsically flame-retardant calcium alginate fibre, Polym. Degrad. Stabil. 96 (5) (May 2011) 936–942, https://doi.org/10.1016/j.polymdegradstab.2011.01.029.
[55] C. Hu, W. Lu, A. Mata, K. Nishinari, Y. Fang, Ions-induced gelation of alginate: mechanisms and applications, Int. J. Biol. Macromol. 177 (Apr. 2021) 578–588, https://doi.org/10.1016/j.ijbiomac.2021.02.086.
[56] H. Malektaj, A.D. Drozdov, J. deClaville Christiansen, Swelling of homogeneous alginate Gels with Multi-stimuli Sensitivity, Int. J. Mol. Sci. 24 (6) (Mar. 2023) 5064, https://doi.org/10.3390/ijms24065064.
[57] S. Kalliola, et al., Carboxymethyl chitosan and its Hydrophobically modified derivative as pH-Switchable Emulsifiers, Langmuir 34 (8) (Feb. 2018) 2800–2806, https://doi.org/10.1021/acs.langmuir.7b03959.
[58] Mathematical models of drug release, in: Strategies to Modify the Drug Release from Pharmaceutical Systems, Woodhead Publishing, 2015, pp. 63–86, https://doi.org/10.1016/b978-0-08-100092-2.00005-9.
[59] L.R. Grace, M.C. Altan, Characterization of anisotropic moisture absorption in polymeric composites using hindered diffusion model, Compos. Appl. Sci. Manuf. 43 (8) (Aug. 2012) 1187–1196, https://doi.org/10.1016/j.compositesa.2012.03.016.
[60] M. Maraldi, A. Guida, M. Sponchioni, D. Moscatelli, Influence of the polymer architecture and Functionalization with carboxylate groups over the release of octenidine Hydrochloride from poly(lactic acid)-based nanoparticles, Macromol. Mater. Eng. 306 (2) (2021) 2000592, https://doi.org/10.1002/mame.202000592.
[61] H.M. Nizam El-Din, A.W.M. El-Naggar, F.I. Abu-El Fadle, Characterization and drug release kinetics of polyacrylamide/sodium alginate blend hydrogels synthesized by gamma irradiation, Polym. Bull. 81 (7) (May 2024) 6149–6171, https://doi.org/10.1007/s00289-023-04991-3.
[62] G. Qipeng, L. Zhenhai, Phase behavior of polymer blends, J. Therm. Anal. Calorim. 59 (1) (Jan. 2000) 101–120, https://doi.org/10.1023/A:1010179711232.
[63] R.K. Farag, R.R. Mohamed, Synthesis and characterization of carboxymethyl chitosan Nanogels for swelling studies and antimicrobial activity, Molecules 18 (1) (Dec. 2012) 190, https://doi.org/10.3390/molecules18010190.
[64] G.D. Mogoşanu, A.M. Grumezescu, Natural and synthetic polymers for wounds and burns dressing, Int. J. Pharm. 463 (2) (Mar. 2014) 127–136, https://doi.org/10.1016/j.ijpharm.2013.12.015.
[65] B. Bayón, I.R. Berti, A.M. Gagneten, G.R. Castro, Biopolymers from Wastes to high-value products in Biomedicine, in: R.R. Singhania, R.A. Agarwal, R.P. Kumar, R. K. Sukumaran (Eds.), Waste to Wealth, Springer Singapore, Singapore, 2018, pp. 1–44, https://doi.org/10.1007/978-981-10-7431-8_1.
[66] N. Joy, S. Samavedi, Identifying specific combinations of matrix properties that promote controlled and sustained release of a hydrophobic drug from Electrospun meshes, ACS Omega 5 (26) (July 2020) 15865–15876, https://doi.org/10.1021/acsomega.0c00954.
[67] S.Y.C. Tong, J.S. Davis, E. Eichenberger, T.L. Holland, V.G. Fowler, Staphylococcus aureus infections: Epidemiology, Pathophysiology, clinical Manifestations, and Management, Clin. Microbiol. Rev. 28 (3) (May 2015) 603–661, https://doi.org/10.1128/cmr.00134-14.